ADVANCED FUNCTIONAL MATERIALS
www.afm-journal.de

Flexible Solid-State Supercapacitor Based on Graphene-based Hybrid Films

*Meng Li, Zhe Tang, Mei Leng, and Junmin Xue**

A flexible solid-state asymmetric supercapacitor based on bendable film electrodes with 3D expressway-like architecture of graphenes and "hard nano-spacer" is fabricated via an extended filtration assisted method. In the designed structure of the positive electrode, graphene sheets are densely packed, and $Ni(OH)_2$ nanoplates are intercalated in between the densely stacked graphenes. The 3D expressway-like electrodes exhibit superior supercapacitive performance including high gravimetric capacitance (≈573 F g^{-1}), high volumetric capacitance (≈655 F cm^{-3}), excellent rate capability, and superior cycling stability. In addition, another hybrid film of graphene and carbon nanotubes (CNT) is fabricated as the negative electrodes for the designed asymmetric device. In the obtained graphene@CNT films, CNTs served as the hard spacer to prevent restacking of graphene sheets but also as a conductive and robust network to facilitate the electrons collection/transport in order to fulfill the demand of high-rate performance of the asymmetric supercapacitor. Based on these two hybrid electrode films, a solid-state flexible asymmetric supercapacitor device is assembled, which is able to deliver competitive volumetric capacitance of 58.5 F cm^{-3} and good rate capacity. There is no obvious degradation of the supercapacitor performance when the device is in bending configuration, suggesting the excellent flexibility of the device.

1. Introduction

Bendable freestanding films emerge to garner major interest recently because they have various potential applications in energy storage,[1] catalysis,[2,3] environment[3] and sensing. Particularly, flexible energy storage devices such as supercapacitors and batteries, which extensively rely on such bendable film electrodes, are receiving more and more attention with the increasing demand for wearable and portable consumer electronics.[4,5] Graphene, a 2D geometric materials associated with numerous advanced properties, is regarded as one of the most suitable candidates to realize such flexible film electrodes.[6,7] In fact, as of now freestanding graphene-based films have shown more applications compared to individual graphene sheets.[8] However, during the fabrication process, freestanding films composed of graphene nanosheets are readily to be restacked into bulk "graphite" due to the strong van der Waals attraction, in which the beauty of the individual graphene sheets, such as high surface area and high flexible ability, will be lost. As a consequence, the electrode performance of the films will be severely affected due to the poor penetration of electrolyte into the graphene nanosheets. Much effort has been spent on developing freestanding graphene-based film electrodes without sacrificing the individual properties of graphene sheets. For instance, graphene aerogels electrode materials[4,9] which were formulated with interconnected 3D porous frameworks of graphene, were reported recently. These graphene aerogel based electrodes had nice features demanded in electrode applications such as large specific surface area, excellent electron conductivity and rapid electrolyte ions diffusion. Although such electrodes offered an impressive gravimetric capacitance of ≈441 F g^{-1} at 1 A g^{-1} in aqueous electrolyte, the volumetric electrochemical performance of these electrodes was not satisfied due to their low packing density. In real industrial applications, volumetric capacitance is more recommended than the widely used gravimetric capacitance to evaluate the electrochemical performance of supercapacitor electrodes. Very recently, a breakthrough of graphene based flexible supercapacitor electrodes was made by Li's group.[10,11] In Li's work, the porous yet densely packed graphene gel film was formed by capillary compression of chemically converted graphene (CCG) in the presence of volatile and nonvolatile liquid electrolyte. The packing density of the obtained graphene film was nearly doubled (≈1.33 g cm^{-3}) in contrast to that of the traditional porous carbon, and the yielded volumetric capacitance can reach 255.5 F cm^{-3} in aqueous electrolyte at low current density of 0.1 A g^{-1}. In this method, it is a successful attempt to enhance the packing density through selected removal of volatile solvent trapped in the film. However, there is little information available in exactly controlling such capillary compression process by using acid aqueous as "soft spacer" under high vacuum condition. Moreover, the graphene gel films are very susceptible to rupture during the tedious preparation processes as a results of their low mechanical strength. Therefore, there is a great urgent need to extend a facile strategy by utilizing "hard" nanomaterials as substitute spacer in order to address the aforementioned issues.

Herein we report the fabrication of a flexible solid-state symmetric supercapacitor based on bendable film electrodes

M. Li, Dr. Z. Tang, Dr. M. Leng, Dr. J. Xue
Department of Materials Science and Engineering
National University of Singapore
Singapore 117573
E-mail: msexuejm@nus.edu.sg

DOI: 10.1002/adfm.201402442

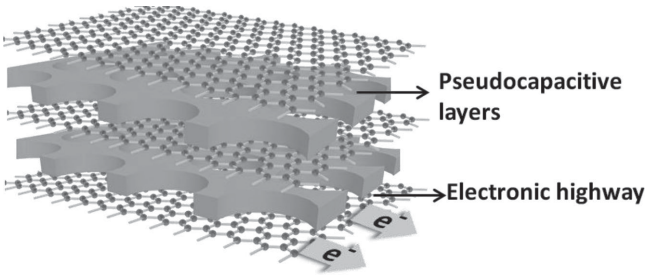

Figure 1. Schematic illustrating advantages of 3D layer-by-layer structure of graphene intercalated with pseudocapacitive layer.

with optimized composite structure of graphenes and "hard nano-spacer" via an extended filtration assisted method. In the designed structure of positive electrode, as illustrated in **Figure 1**, graphene sheets were densely packed, and $Ni(OH)_2$ nanoplates were intercalated in between the densely stacked graphenes. Although similar idea and scheme have been proposed by many groups in recent years,[7,12] very few state-of-the-art hybrid electrodes can realize the ideal intercalated structure with densely packed graphene layers. Among numerous metal oxide/hydroxide electrode materials,[13,14] $Ni(OH)_2$ was chosen here in terms of its high capacitance value (up to 3000 F g^{-1}),[15] easy fabrication, suitable particle size and low cost. $Ni(OH)_2$ nanoplates act not only effective space inhibitor to prevent graphene restacking but also pseudocapacitor to improve the overall capacitance, while the highly conductive graphene nanosheets serve as expressway for efficient electronic transportation. Furthermore, the graphene nanosheets also keep the integrity of the film and offer flexibility. With regard to the negative electrode, carbon nanotube (CNT) was served as hard spacer in order to fulfill the demand of high-rate performance of the asymmetric supercapacitor. Such asymmetric system is expected to possess the advantages of both capacitors and batteries. The combination of two different type of electrode would result in a much enhanced energy storage capability without sacrificing the superior power delivery properties of traditional supercapacitors. The obtained flexible solid-state supercapacitor based on both 3D expressway-like film electrodes was expected to have superior performance in terms of capacitance (both volumetric and gravimetric performance) and rate capability.

2. Results and Discussion

2.1. Positive Electrode

The proposed bendable positive electrode was fabricated via a filtration assisted layer by layer self-assembly route as illustrated in Figure S1,S2 (Supporting Information). The morphology and structure characterizations of the as-prepared graphene@$Ni(OH)_2$ films (GNiF) are presented in **Figure 2**. For comparison, the SEM and TEM images of bare $Ni(OH)_2$ nanoplates are shown in Figure S3 (Supporting Information). The synthesized $Ni(OH)_2$ nanoplates show a uniform hexagonal morphology with a typical thickness around 20 nanometers and a side length of several hundred nanometers. Then conformal synthesis of the $Ni(OH)_2$ nanoplates guaranteed a uniform intercalation into the dense graphene layers as can be seen in Figure 2a,c. In addition, the closely stacked graphene sheets become flexible and much more porous when numerous $Ni(OH)_2$ nanoplates are presented in between (Figure 2a Inset). Figure 2d shows the cross sectional SEM image of the GNiF film, which was performed through ion beam milling. The notch drilled in the film was 5 μm in width and 6 μm in depth. Uniform distribution of the $Ni(OH)_2$ nanoplates in between the graphene layers is clearly shown in the image. Moreover, the in-plane viewe of the film (Figure 2e and the inset) further indicate the excellent distribution of $Ni(OH)_2$ nanoplates between the graphene sheets. The crystal structure of the as-prepared films was studied using X-ray diffraction (XRD, Figure 2f left), where the peaks could be indexed to β-$Ni(OH)_2$ (JCPDF: 14–0117). The X-ray photoelectron spectroscopy (XPS) spectrum of GNiF is shown in the right side of Figure 2f, and the spectrum of GNiF without annealing was also collected as a control. In the sample of GNiF without annealing, the XPS spectrum of C 1s was deconvoluted into three peaks (colored lines) with different relative carbon contents: sp^2 bonded carbon at 284.5 eV (C–C, 46.48%), hydroxyls at 286.5 eV (C–O, 45.52%), carbonyls at 288.1 eV (C = O, 8.01%). This result reveals the high percentage of oxygen-contained functional groups before annealing. In contrast, the C–O and C = O peaks of the annealed GNiF are dramatically decreased to 13.86% and 5.86%, respectively, and the content of sp^2 bonded carbon is increased to 80.28%. These results suggest that GO in the hybrid film is effectively reduced upon annealing at 300 °C. The effective reduction will significantly enhance the conductivity of the as-obtained freestanding film electrode.

In the 3D expressway-like graphene@$Ni(OH)_2$ hybrid films, the $Ni(OH)_2$ nanoplates and optimized graphene sheets can offer a short diffusion pathway for both electron transportation and electrolyte penetration. Meanwhile, numerous slit-like pores derived from the homogeneously dispersed $Ni(OH)_2$ nanoplates can provide a huge accumulation place for electrolyte ions and allow a high loading amount of energy. These advantages will ultimately result in a remarkably enhanced energy storage performance. Compared with the previously reported graphene@$Ni(OH)_2$ composites,[16–18] such hybrid film has several advantages: i) the layer-by-layer structure is able to inhibit the aggregation of the graphene sheets effectively; ii) the stacked graphene sheets will uttermost maintain their integrity and flexibility; iii) the densely packed hybrid films is significantly competitive in the volumetric performance of the freestanding film electrode. Such graphene@$Ni(OH)_2$ hybrid film provides an ideal structural model for combining both electrochemical double-layer capacitive materials and pseudocapacitive materials.

A pure graphene film without intercalation of $Ni(OH)_2$ nanoplates was also prepared as a comparison. The SEM result of the pure graphene film in Figure S4 (Supporting Information) clearly shows an extremely densely packed graphene film where diffusion and penetration of electrolyte would be hard to take place. In order to verify the universality of this approach, another 1-D metal oxide, TiO_2 nanobelts, was also employed into the same fabrication process. Interestingly, the as-obtained hybrid graphene@TiO_2 film (Figure S5, Supporting Information) shows the similar wrinkled lamellar structure of stacked

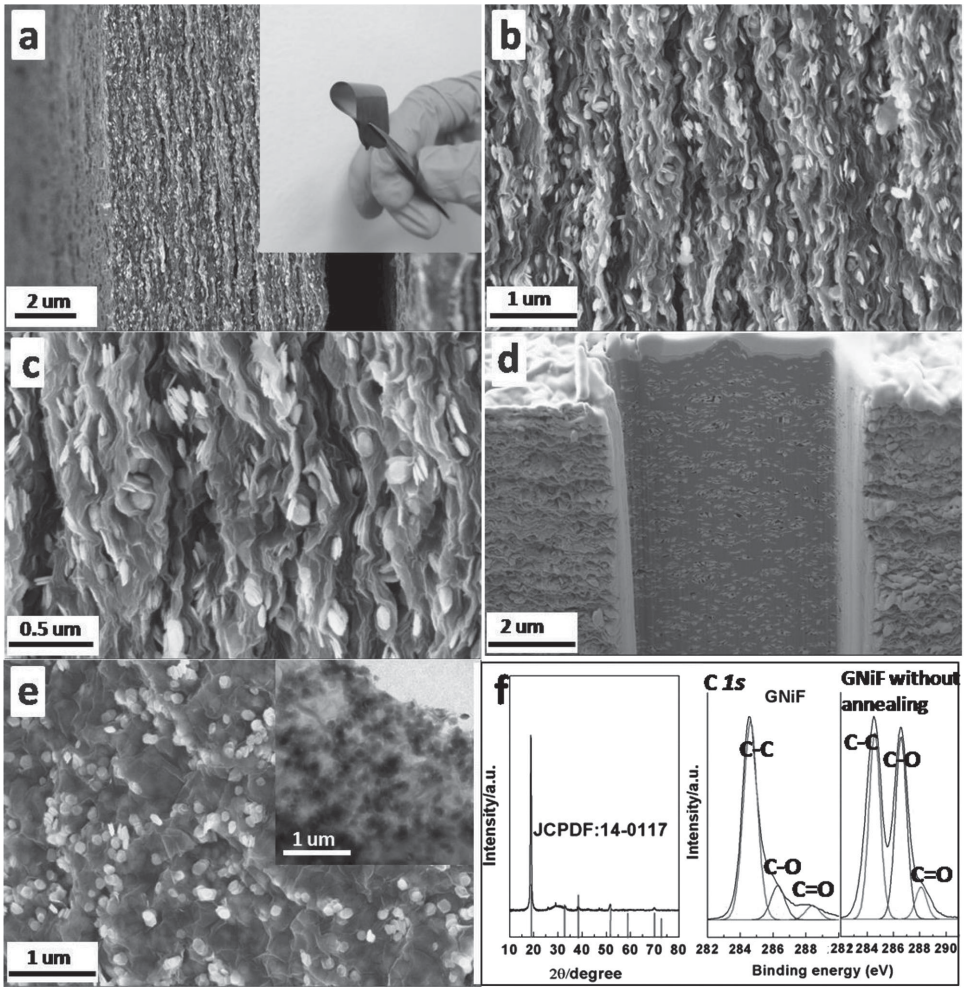

Figure 2. Morphologies and structure characterizations of 3D dense graphene films intercalated with $Ni(OH)_2$ nanoplates. a–c) cross sectional SEM images of GNiF at different magnifications, inset optical image of GNiF showing its flexibility; d) side view of the focused-ion beam (FIB)-etched GNiF in parallel direction to the graphene sheets; e) In-plane viewed SEM and TEM (inset) images of GNiF in perpendicular direction to the graphene sheets; f) XRD patterns (left) and XPS carbon core level XPS spectra (right) of GNiF.

graphene sheets embedded with TiO_2 nanobelts, which would be a promising candidate in the field of catalysis and solar energy devices.

The electrochemical tests of the as-obtained hybrid film were first performed in a three-electrode cell (**Figure 3**), in which a platinum foil and a saturated calomel electrode (SCE) were used as the counter and reference electrodes, respectively. The cyclic voltammetry (CV) curves of GNiF electrode measured at different scan rates showed characteristic symmetric redox peaks of β-$Ni(OH)_2$, indicating a good reversibility of the electrode. These redox peaks are corresponding to the Faradaic reactions of β-$Ni(OH)_2$: $Ni(OH)_2 + OH^- \rightleftharpoons NiOOH + H_2O + e^-$. Additionally, the electrochemical response current increases with increasing scan rate, and the CV curves almost keep the same profiles with slightly shift of peak positions, suggesting the superior electronic conduction within the layer by layer structured electrode. To further quantify the capacitance of the as-obtained hybrid film electrode, a series of galvanostatic charge–discharge measurements were carried out at different current densities, and the typical discharge curves are presented in Figure 3b. In contrast to the linear characteristic of EDLC electrodes, the GNiF electrode demonstrated a distinct plateau in the discharge curves, suggesting its pseudocapacitive behavior, which is in good agreement with their CV results. Moreover, the gravimetric and volumetric capacitance of GNiF electrode at different current densities were calculated (based on the total mass of electrode, graphene + $Ni(OH)_2$) from the discharge curves and the results are shown in Figure 3c. As shown in Figure 3c (right *Y* axis in Figure 3c), the GNiF electrode was able to yield a high gravimetric capacitance of 573 F g^{-1} at 0.2 A g^{-1} based on the total electrode mass. When the current density was increased to 50 A g^{-1}, its capacitance remained at 413.5 F g^{-1}, corresponding to a capacitance loss of only 27.7% compared to its initial value while the current density was increased 250 times. This result is comparable to those previously reported as shown in **Table 1**.[15–17,19] For example, Wei et al.[17] reported a hierarchical flowerlike nickel hydroxide decorated on graphene sheets with a capacitance of 1735 F g^{-1} at a low scan rate of 1 mV s^{-1}. However, the capacitance dramatically decreased to 523 F g^{-1} when the scan rate increased

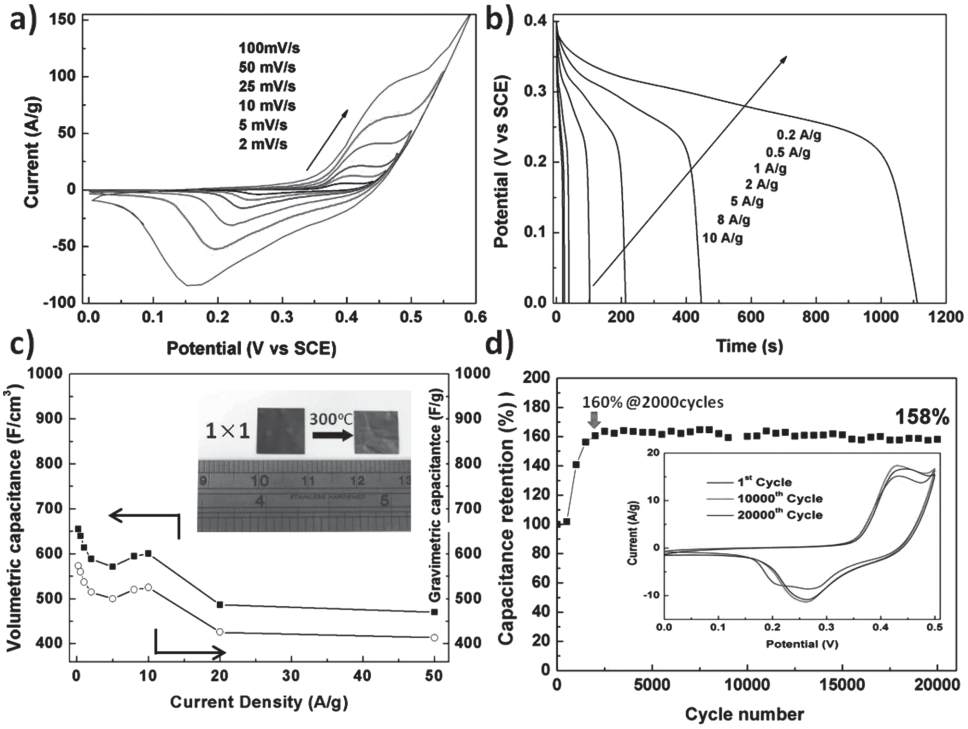

Figure 3. Electrochemical performance of GNiF electrode in a three-electrode configuration. a) CV measured at different scan rates; b) Galvanostatic discharge curves at various current density; c) Variation of gravimetric capacitance and volumetric capacitance (based on the total mass of $Ni(OH)_2$ and graphene) of GNiF electrode as a function of current density. Inset optical image shows the shrinkage of hybrid film electrode after annealing; d) Cyclability of the GNiF electrode in a 1 M KOH electrolyte. Inset shows CV variation after 20000 cycles at the scan rate of 10 mV s^{-1}.

to 50 mV s^{-1}, suggesting a capacitance loss as high as 70% with 50 times scan rate increasing. Moreover, the GNiF electrode also exhibited a comparable rate capacity even compared with the pure graphene films reported in reference [7]: When the current density was increased from 0.1 A g^{-1} to 50 A g^{-1}, the capacitance loss was 21.3% for EM-CCG, similar to our result of 27.7%. This is a quite a competitive feature considering its capacitance improvement over the pure carbon electrodes.

As some researchers such as Li, Gogotsi and Simon pointed out volumetric performance was more recommended than widely used gravimetric ones in their recent studies,[10,20] GNiF electrodes were also evaluated as volumetric (left *Y* axis in Figure 3c). The inset optical image in Figure 3c shows the shrinkage of hybrid film electrode after annealing. The volumetric shrinkage leads to a more densely packed hybrid film, and the densely packed graphene/$Ni(OH)_2$ electrode will ultimately result in a high volumetric performance. As expected, the volumetric capacitance of GNiF electrode is as high as 655 F cm^{-3} at a current density of 0.2 A g^{-1}, which is visibly advantageous in contrast to ≈275 F cm^{-3} of EM-CCG[10] at 0.1 A g^{-1} reported recently. The superior electrochemical performance of the hybrid freestanding film highlights the advantages of layer by layer structured film, which can be accounted for that 3D expressway-like structure provide efficient and fast diffusion pathway of electrolyte ions to the active material surface and excellent electron transport within the graphene layers.

The stability is also a key parameter to evaluate the performance of an electrode material. Thus the cycle life test of

Table 1. Gravimetric capacitance retention of GNiF electrode compared with some $Ni(OH)_2$/Carbon electrodes reported in previous literatures.

Materials	Initial rate – Specific capacitance	Final rate – Specific capacitance	Final rate/Initial rate	Capacitance Loss	Ref.
GNiF	0.2 A/g – 573 F/g	50 A/g – 413 F/g	250	27.7%	Present Work
$Ni(OH)_2$/graphene	1 mV/s – 1735 F/g	50 mV/s – 523 F/g	50	70%	[11b]
$Ni(OH)_2$/CNT/NF	2.5 mA/cm^{2-} 3166 F/g	50 mA/cm^{2-} 2102 F/g	20	33%	[10]
$Ni(OH)_2$-Ni foam	4 A/g – 3152 F/g	16 A/g – 280 F/g	4	91%	[12a]
$Ni(OH)_2$/UGF	0.5 A/g – 166 F/g	10 A/g – 116 F/g	20	30%	[12b]
Amorphous $Ni(OH)_2$	1 mV/s – 2188 F/g	20 mV/s – 1250 F/g	20	42.9%	[12c]
$Ni(OH)_2$/graphene	2.8 A/g – 1335 F/g	45.7 A/g – 953 F/g	16.3	28.6%	[11a]
EM-CCG	0.1 A/g – 203.2 F/g	50 A/g – around 160 F/g	500	21.3%	[7a]

the GNiF electrode was carried out for 20 000 cycles and the result is presented in Figure 3d. The results indicated that the capacitance retention was not stumbling over the long term cycling, but even increased by 58% of its initial capacitance. Such excellent performance could be attributed to the lamellar structure of densely packed graphene@$Ni(OH)_2$ nanoplates films. To be specific, the majority of capacitance increase (160%) happened in the first 2000 cycles, which could be due to the activation of oxides and dense films that allows trapped ions to penetrate more freely. In fact, the activation mechanism can be divided into two parts: the electrolyte ions make transportation more smoothly in the initially blocked area between the dense graphene layers due to long term cycling; the trapped ions between the $Ni(OH)_2$ crystalline layers during the growth of nanoplates can diffuse more freely after extended cycling. The CV curves of the electrode at the 1st, 10 000th, and 20 000th cycles at the scan rate of 10 mV s^{-1} are shown in inset of Figure 3d. Three CV curves exhibit similar profiles with a pair of oxidation/reduction peaks. However, the redox peaks after extended cycling were better defined and the potential differences between the two peaks are slightly increased[21] from 0.18 V (initial cycle) to 0.21 V (final cycle). The relatively small potential difference indicates a good reversibility of the redox reaction for the GNiF electrode. It is notable that the CV curve of the 20 000th cycle almost overlapped with that of 10 000th cycle, revealing an extraordinary stability of the GNiF electrode. To restate, such excellent cycling performance benefits from the following factors: 1) the layered carbon matrix is able to effectively buffer the stress and strain related to the $Ni(OH)_2$ nanoparticles volume contraction/expansion during long term charging-discharging; 2) the densely packed yet porous graphene architecture provide a high contact area between electrolyte and electrode, and each $Ni(OH)_2$ nanoplate is held in position by graphene layers, preventing them from agglomeration upon cycling. The morphology of such hybrid film electrode after long term electrochemical cycling is presented in Figure S7. The cross-sectional images in Figure S7a show the stacked graphene sheets embedded by $Ni(OH)_2$ having with more porosities than the original one. The in-plane viewed images (Figure S7b, Supporting Information) exhibit wrinkled surface with more roughness due to the long term incorporation with electrolyte.

2.2. Negative Electrode

In order to fulfill the high-power characteristic of an asymmetric supercapacitor, a CNT backbone was selected to intercalate into the graphene nanosheets as a conductive and robust network to facilitate the electrons collection/transport in the negative electrode. CNT has been widely regarded as the choice of high-power electrode material owing to its improved electrical conductivity and high readily accessible surface area.[22,23] Similar to the positive GNiF electrode, CNTs were incorporated in between the densely stacked graphene as illustrated in **Figure 4**a. The inner structure of this hybrid graphene@CNT film (GTF) is presented in Figure 4b–d. The average thickness of the GTF was around 7.4 μm showing a highly bendable feature. The high resolution SEM (Figure 4c) and FIB image (Figure 4d) clearly reveal the uniform distribution of the CNTs in between the graphene layers. The XPS spectrum of the GTF in Figure 4e indicates that GO has been effectively reduced to graphene by hydrazine. The electrochemical evaluation of the GTF was performed in a three-electrode configuration. As shown in Figure 4f, the GTF negative electrode exhibited an ideal rectangular shaped CV at various sweep rates, indicating the favorable capacitive behavior. Moreover, the symmetric charge–discharge profiles in Figure 4g suggest its typical EDLC storage mechanism. The specific capacitances calculated from the discharge curves were 154 and 152 F g^{-1} at the current densities of 1 and 2 A g^{-1}, respectively. The overall capacitive performance of the GTF is presented in Figure 4h. The corresponding volumetric capacitance of the GTF electrode was calculated to be 192.5 F cm^{-3} at 1 A g^{-1}, which is almost same performance in contrast to ≈226.9 F cm^{-3} of EM-CCG[10] at 1 A g^{-1} reported recently. Its highly volumetric capacitance can be probably accounted for its densely packed yet porous architecture where a high contact area between the electrolyte and electrode was assured. The result of cycling stability for the GTF electrode is shown in the inset of Figure 4h. It can be seen in Figure 4h that after 2000 cycles, 89% of its initial capacitance was remained, suggesting its good cycling stability. The impressive performances of GTF negative electrode can be accounted for the similar advantages as positive electrode: i) the intercalated CNTs are able to inhibit the aggregation of the graphene sheets effectively; ii) the robust network of CNT backbone will greatly improve the flexibility and strength of the GTF; iii) the densely packed hybrid films is significantly competitive in the volumetric performance of the freestanding film electrode.

2.3. Solid-State Flexible Supercapacitor

To further investigate the capacitive performance of the as-obtained flexible electrodes in a full cell set-up, a solid-state asymmetric supercapacitor is assembled in our study by using a GNiF as the positive electrode and a GTF as the negative electrode. Gel electrolyte of Polyvinyl alcohol (PVA)/KOH system was used in this study. In contrast to liquid-based supercapacitors, this solid-state device has several advantages such as flexibility, ease of fabrication, wide working temperature and improved safety. As for a full cell supercapacitor, the charge balance should follow the relationship of $q_+ = q_-$. Thus the mass balance between the negative electrode and positive electrode will follow the equation:[13] $m_-/m_+ = (C_+ \times \Delta E_+)/(C_- \times \Delta E_-)$, where m is the mass of electrode, C is the specific capacitance and ΔE is the potential range for the charge/discharge process. Accordingly, the optimized mass ratio between the negative and positive electrodes should be m(GTF)/m(GNiF) = 1.8 in the asymmetric supercapacitor full cell. **Figure 5**a shows the assembled flexible solid-state supercapacitor with an electrode area of 2 cm × 4 cm (around 3 mg cm^{-2} based on the mass of electrode materials). Figure 5b illustrates the CV curve of the flexible solid-state supercapacitor at various scan rates in a wide potential window range from 0 to 1.7 V. Unlike the sharp redox peaks present in the positive electrode,

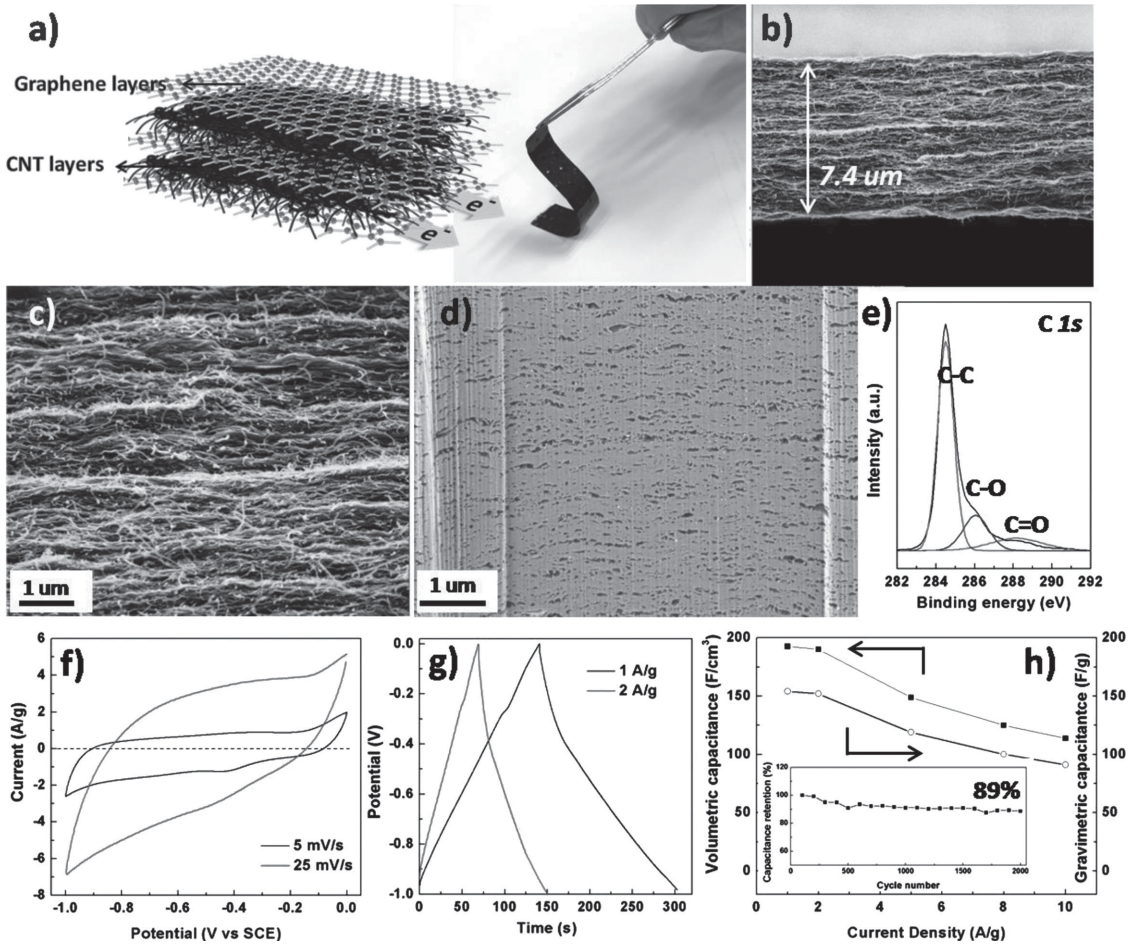

Figure 4. a) schematic illustration of layered structure for GTF material and optical image of GTF showing its flexibility; b), c) cross sectional SEM images of GTF at various magnifications; d) side view of the FIB-etched GTF; e) XPS spectra f) CV measured at different scan rates g) galvanostatic charge–discharge curves at various current density of GTF; h) variation of gravimetric and volumetric capacitance of GTF as a function of current density, inset shows the cyclability of GTF electrode in 1 M KOH electrolyte.

this full cell flexible supercapacitor shows a quasi-rectangular CV curve, suggesting a pseudo-constant charge/discharge rate process over the entire CV cycle.[23] Moreover, the galvanostatic charge–discharge curve at a current density of 1A g^{-1} (Figure 5c inset) exhibits almost a linear variation and a symmetrical shape with a quick *I–V* response, which is consistent with the CV result and further revealing its capacitor-like behavior. The calculated specific gravimetric capacitances based on the total mass of the positive and negative electrodes at 1, 5, 10, and 20 A g^{-1} are 44.8, 34.7, 22.2, and 15.9 F g^{-1}, which are shown in Figure 5c. The volumetric capacitances based on the total volume of both electrodes are 58.5, 45.2, 28.9, and 21 F cm^{-3}. However, it was noted that the capacitance loss of the solid-state supercapacitor was 64.5% when the current density was increase from 1 to 20 A g^{-1}, which was unexpected considering that the superior rate capacity of the positive electrode shown in Table 1. It is very likely that the rate capacity of the full cell was undermined by the poor ionic conductivity of solid electrolyte and the relatively slow rate of surface reaction between the electrode and gel electrolyte under high current density. Nevertheless, some organic and ionic liquid electrolytes were attempted to be utilized in order to optimize the performance of the full cell supercapacitor. The Ragone plot derived from the discharge curves at various current densities is shown in Figure S8. At a low current density of 1 A g^{-1}, the corresponding energy density and power density are 18 Wh kg^{-1} and 850 W kg^{-1}, respectively. When the current density is increased to 20 A g^{-1}, the corresponding energy density remains at 6.4 Wh kg^{-1} at a high power density of 17 kW kg^{-1}. The influence of bending on the electrochemical performance was also conducted on the flexible solid-state device. As shown in Figure 5d, no obvious change of the as-measured CV curves was observed when the cell was even bended to 180°. This excellent flexibility opens much more opportunities for the GNiF/GTF-based solid-state supercapacitor in a wide range of applications.

3. Conclusions

In summary, several freestanding hybrid films were fabricated by extended filtration method via self-assembly of graphene

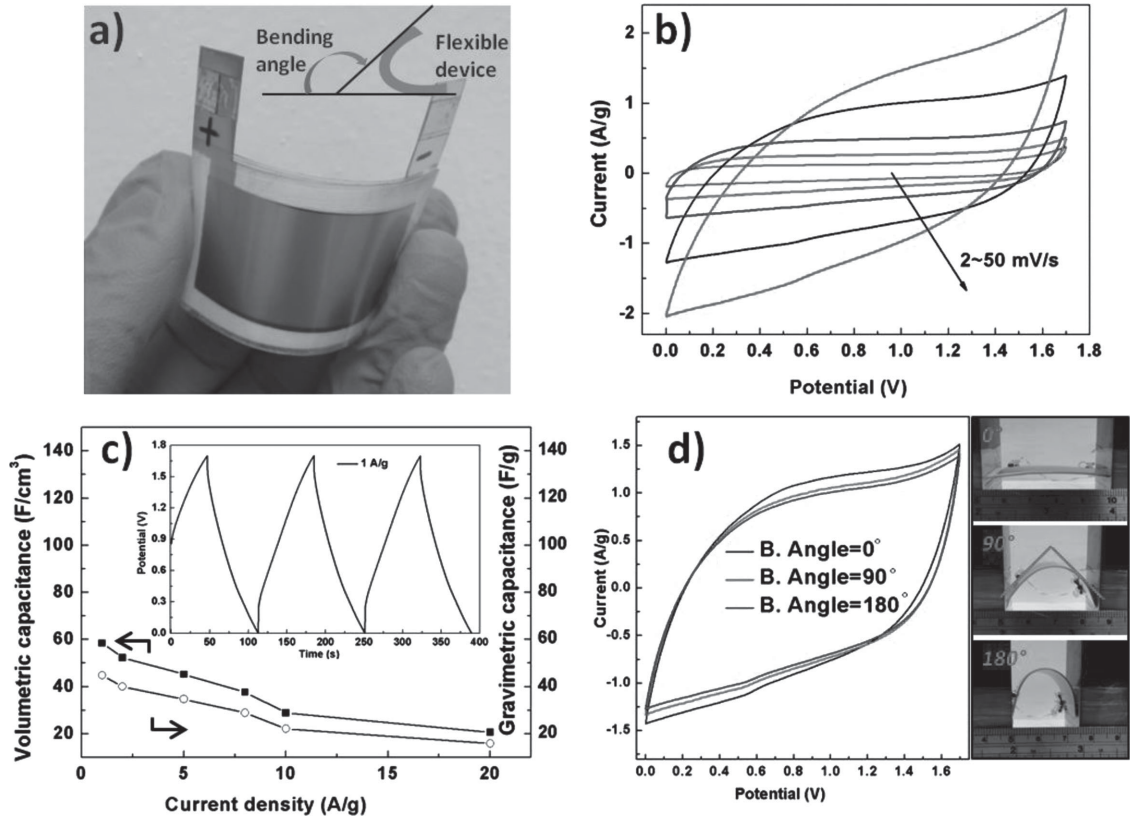

Figure 5. Electrochemical performance of GNiF//GTF asymmetric supercapacitor. a) Optical photographs of the fabricated flexible solid-state supercapacitor device with electrode area of 2 cm × 4 cm, inset shows the schematic definition of bending angle; b) CV measured at various scan rate; c) Variation of volumetric and gravimetric capacitance (based on the total mass of positive and negative electrodes) as a function of scan rate, inset shows the galvanostatic charge–discharge curve at the current density of 1 A g^{-1}; d) CV curves measured at different curvatures of 0°, 90°, and 180°, right inset shows the optical images of as-obtained flexible supercapacitor in different bending states.

sheets and "hard nano-spacer" including $Ni(OH)_2$ nanoplates, TiO_2 nanobelts and CNT. The structure characterizations of SEM, TEM and FIB images confirmed that these nano-spacers were uniformly dispersed in the hybrid films, serving as effective inhibitors of aggregation in between the graphene layers. These advantageous features demonstrate that such 3D expressway-like hybrid films could be an ideal candidates for flexible energy storage devices. The electrochemical performance of GNiF electrodes exhibit high gravimetric capacitance, high volumetric capacitance, excellent rate capability and superior cycling stability. Furthermore, a flexible solid-state supercapacitor with an asymmetric configuration was developed based on the GNiF and GTF electrodes. This solid-state supercapacitor showed several superior properties such as high flexibility, high volumetric capacitance (58.5 F cm^{-3}) and good rate capacity (energy density remained at 9 Wh kg^{-1} at a high power density of 8500 W kg^{-1}). Further optimization of both the electrode and electrolyte is under way to improve the performance of the solid-state supercapacitor. We believe that our solid-state supercapacitor prototype utilizing such bendable film electrodes in non-aqueous electrolytes can provide a promising route to fabricating highly compact energy storage devices with high energy densities and excellent stability.

Supporting Information

Supporting Information is available from the Wiley Online Library or from the authors.

Acknowledgements

The authors thank the financial support provided by Singapore MOE Tier 1 funding R-284–000–124–112. The authors are also grateful to Eugene Shi Guang Choo, staff of ZEISS Advanced Imaging Centre (Singapore), who did the FIB cross-sectioning and imaging of the graphite composite materials.

Received: July 22, 2014
Revised: August 17, 2014
Published online: September 12, 2014

[1] S. Yin, Y. Goldovsky, M. Herzberg, L. Liu, H. Sun, Y. Zhang, F. Meng, X. Cao, D. D. Sun, H. Chen, A. Kushmaro, X. Chen, *Adv. Funct. Mater.* **2013**, *23*, 2972.

[2] I. Y. Kim, S. Park, H. Kim, S. Park, R. S. Ruoff, S.-J. Hwang, *Adv. Funct. Mater.* **2013**, *24*, 2288.

[3] a) F. Schedin, A. K. Geim, S. V. Morozov, E. W. Hill, P. Blake, M. I. Katsnelson, K. S. Novoselov, *Nat. Mater.* **2007**, *6*, 652; b) D. Cohen-Tanugi, J. C. Grossman, *Nano Lett.* **2012**, *12*, 3602.

[4] Y. Xu, Z. Lin, X. Huang, Y. Wang, Y. Huang, X. Duan, *Adv. Mater.* **2013**, *25*, 5779.
[5] a) Q. Cao, H.-s. Kim, N. Pimparkar, J. P. Kulkarni, C. Wang, M. Shim, K. Roy, M. A. Alam, J. A. Rogers, *Nature* **2008**, *454*, 495; b) S. Ju, A. Facchetti, Y. Xuan, J. Liu, F. Ishikawa, P. Ye, C. Zhou, T. J. Marks, D. B. Janes, *Nat. Nanotechnol.* **2007**, *2*, 378.
[6] Y. Meng, K. Wang, Y. Zhang, Z. Wei, *Adv. Mater.* **2013**, *25*, 6985.
[7] J. Xie, X. Sun, N. Zhang, K. Xu, M. Zhou, Y. Xie, *Nano Energy* **2013**, *2*, 65.
[8] a) X. Yang, J. Zhu, L. Qiu, D. Li, *Adv. Mater.* **2011**, *23*, 2833; b) X. Yang, L. Qiu, C. Cheng, Y. Wu, Z.-F. Ma, D. Li, *Angew. Chem. Int. Ed.* **2011**, *50*, 7325.
[9] a) L. Zhang, X. Yang, F. Zhang, G. Long, T. Zhang, K. Leng, Y. Zhang, Y. Huang, Y. Ma, M. Zhang, Y. Chen, *J. Am. Chem. Soc.* **2013**, *135*, 5921; b) Y. Zhao, J. Liu, Y. Hu, H. Cheng, C. Hu, C. Jiang, L. Jiang, A. Cao, L. Qu, *Adv. Mater.* **2013**, *25*, 591; c) Y. Xu, Z. Lin, X. Huang, Y. Liu, Y. Huang, X. Duan, *ACS Nano* **2013**, *7*, 4042.
[10] X. Yang, C. Cheng, Y. Wang, L. Qiu, D. Li, *Science* **2013**, *341*, 534.
[11] M. D. Stoller, S. Park, Y. Zhu, J. An, R. S. Ruoff, *Nano Lett.* **2008**, *8*, 3498.
[12] a) S. J. R. Prabakar, Y.-H. Hwang, E.-G. Bae, S. Shim, D. Kim, M. S. Lah, K.-S. Sohn, M. Pyo, *Adv. Mater.* **2013**, *25*, 3307; b) Z.-S. Wu, G. Zhou, L.-C. Yin, W. Ren, F. Li, H.-M. Cheng, *Nano Energy* **2012**, *1*, 107.
[13] Z. Fan, J. Yan, T. Wei, L. Zhi, G. Ning, T. Li, F. Wei, *Adv. Funct. Mater.* **2011**, *21*, 2366.
[14] a) Y. Wang, Y. Xia, *Adv. Mater.* **2013**, *25*, 5336; b) H. Chen, L. Hu, Y. Yan, R. Che, M. Chen, L. Wu, *Adv. Energy Mater.* **2013**, *3*, 1636.
[15] Z. Tang, C.-h. Tang, H. Gong, *Adv. Funct. Mater.* **2012**, *22*, 1272.
[16] H. Wang, H. S. Casalongue, Y. Liang, H. Dai, *J. Am. Chem. Soc.* **2010**, *132*, 7472.
[17] J. Yan, Z. Fan, W. Sun, G. Ning, T. Wei, Q. Zhang, R. Zhang, L. Zhi, F. Wei, *Adv. Funct. Mater.* **2012**, *22*, 2632.
[18] F. Zhang, D. Zhu, X. a. Chen, X. Xu, Z. Yang, C. Zou, K. Yang, S. Huang, *Phys. Chem. Chem. Phys.* **2014**, *16*, 4186.
[19] a) G.-W. Yang, C.-L. Xu, H.-L. Li, *Chem. Commun.* **2008**, 6537; b) J. Ji, L. L. Zhang, H. Ji, Y. Li, X. Zhao, X. Bai, X. Fan, F. Zhang, R. S. Ruoff, *ACS Nano* **2013**, *7*, 6237; c) H. B. Li, M. H. Yu, F. X. Wang, P. Liu, Y. Liang, J. Xiao, C. X. Wang, Y. X. Tong, G. W. Yang, *Nat. Commun.* **2013**, *4*, 1894.
[20] Y. Gogotsi, P. Simon, *Science* **2011**, *334*, 917.
[21] G. Zhang, W. Li, K. Xie, F. Yu, H. Huang, *Adv. Funct. Mater.* **2013**, *23*, 3675.
[22] a) Q. Cheng, J. Tang, J. Ma, H. Zhang, N. Shinya, L.-C. Qin, *Phys. Chem. Chem. Phys.* **2011**, *13*, 17615; b) Y. Wimalasiri, L. Zou, *Carbon* **2013**, *59*, 464.
[23] J. Zhao, J. Chen, S. Xu, M. Shao, Q. Zhang, F. Wei, J. Ma, M. Wei, D. G. Evans, X. Duan, *Adv. Funct. Mater.* **2014**, *24*, 2938.